Engineering Structures 274 (2023) 115165

Contents lists available at ScienceDirect

Engineering Structures

journal homepage: www.elsevier.com/locate/engstruct

Estimation of input energy spectrum from pseudo-velocity response spectrum incorporating the influences of magnitude, distance, and site conditions

Haizhong Zhang, Yan-Gang Zhao, Fang-Wen Ge [*], Yingchi Fang, Tsutomu Ochiai

Department of Architecture, Kanagawa University, Yokohama 221-8686, Japan

ARTICLE INFO

Keywords:
Input energy spectrum
Energy equivalent velocity spectrum
Pseudo-velocity response spectrum
Energy-based seismic design

ABSTRACT

The input energy spectrum is useful information for determining the hysteretic energy demand in energy-based seismic design. The input energy spectrum commonly expressed in terms of the energy equivalent velocity spectrum, V_{eq}, can be easily established from the code-specified response spectra (RS) based on the relationship between V_{eq} and RS. Several formulations for the V_{eq}-RS relationship have been developed; however, all of them ignore the influences of magnitude, distance, and site conditions. The aim of this study is to propose a practical formulation for the relationship between V_{eq} and the pseudo-velocity response spectrum, RS_{pv}, incorporating the influences of magnitude, distance, and site conditions. Firstly, to explore the influences of magnitude, distance, and site conditions on the V_{eq}-RS_{pv} relationship, an approach for estimating V_{eq}/RS_{pv} is proposed based upon random vibration theory and verified by comparison with the values calculated by traditional time-series analysis. It is found that the magnitude influences V_{eq}/RS_{pv} the most among these parameters by changing the frequency content of the ground motion, and the V_{eq}/RS_{pv} values at long oscillator periods decrease significantly with an increasing magnitude. Then, based on these conclusions, a practical V_{eq}/RS_{pv} formulation incorporating the influences of magnitude, distance, and site conditions was developed using 16,660 real seismic ground motions in Japan.

1. Introduction

Force- or displacement-based seismic design approaches in current seismic codes have been widely used in structural design for several decades. Nevertheless, since Housner [1] introduced the energy concept in structural seismic design, the energy-based seismic design (EBSD) approach has become increasingly popular [2,3] and was incorporated into the Japanese Building Standard [4]. In contrast to the traditional force- or displacement-based seismic design that uses the peak force or displacement to quantify the destructive potential, the EBSD adopts energy as a performance indicator and can better assess the cumulative damage caused by the cyclic inelastic response. The criterion of EBSD is to keep the structural energy absorption capability greater than the earthquake energy input into a structure. Therefore, the two fundamental works for establishing an EBSD approach are the estimation of the structural energy absorption capability and earthquake energy input into a structure.

Actually, a part of the earthquake energy input into a structure is dissipated by the structural damping, whereas the other is dissipated by the cumulative plastic deformation; only the energy dissipated by the cumulative plastic deformation directly contributes to the cumulative damage. Therefore, EBSD typically uses the hysteretic energy spectrum, E_H, to characterize the earthquake energy demand. To construct E_H for EBSD, many studies prefer to first determine the input energy spectrum, E_I, then obtain E_H based on a hysteretic-to-input energy ratio spectrum E_H/E_I considering the structural damping and hysteretic behavior. Because E_I is a highly stable parameter for characterizing the earthquake energy imparted into a structure, which is primarily determined by the structural mass and natural period and is typically uncoupled with the hysteretic properties of the structure. Many studies [5–10] have focused on establishing an E_I corresponding to a specific return period, which is commonly expressed in forms of the energy equivalent velocity spectrum, V_{eq}, ($V_{eq} = (2E_I/m)^{0.5}$) to remove the effect of the structural mass m. In principle, V_{eq} corresponding to a specific return period can be determined using a traditional approach based on probabilistic seismic hazard analysis (PSHA), similar to the determination of the design

---

[*] Corresponding author.
E-mail address: gefangwen@outlook.com (F.-W. Ge).

https://doi.org/10.1016/j.engstruct.2022.115165
Received 25 May 2022; Received in revised form 27 September 2022; Accepted 17 October 2022

response spectra (RS). Specifically, this approach includes the following steps: (1) identification of all earthquake sources capable of producing damaging ground motions and their probability characteristics, (2) establishment of regional attenuation models for E_I or V_{eq} [11–17], (3) conduction of PSHA considering all the earthquake sources, and (4) determination of spectral shape and scale factor for the design V_{eq} [18–25].

To avoid this complex procedure, some studies [11,26] have tried to directly establish V_{eq} from the RS specified in seismic codes based on the relationship between V_{eq} and RS. To this end, Alici and Sucuoğlu [11] developed a formulation to relate V_{eq} to the pseudo-velocity response spectrum, RS_{pv}, based on a statistical analysis of 104 earthquakes in the Next Generation Attenuation (NGA) database. This formulation was developed as a function of structural damping ratio and period. Du et al. [26] theoretically developed a formulation to relate V_{eq} and the pseudo-acceleration response spectrum, RS_{pa}, based on the earthquake response analysis of a single-degree-of-freedom (SDOF) system in frequency domain. This formulation is a function of the structural damping ratio and period as well as the ground-motion characteristic period, T_g, defined by the ATC [27]. Akiyama and Kitamura [28] discussed the relationship between V_{eq} and the velocity response spectrum, RS_v, and developed a simple RS_v/V_{eq} formulation based on a harmonic seismic response. This formulation includes the structural damping ratio and ground motion duration. Chapman [13] compared the attenuation properties of V_{eq} and RS_{pv} based on 23 earthquakes in western North America and pointed out that the ratio V_{eq}/RS_{pv} is dependent on the magnitude and distance. Merter [29] discussed the relationship between the maximum values of V_{eq} and RS_{pv} based on 100 seismic records from the database of Pacific Earthquake Engineering Research Center (PEER). These studies have made significant contributions to clarifying the relationship between V_{eq} and RS; however, all the current formulations for the V_{eq}-RS relationship ignore the influences of magnitude, distance, and site conditions.

The aim of this study is to (1) clarify the influences of magnitude, distance, and site conditions on the V_{eq}-RS_{pv} relationship and (2) propose a practical formulation for V_{eq}/RS_{pv} incorporating these influences. The rest of this paper is arranged as follows. Section 2 reviews the existing formulations for the V_{eq}-RS relationship. Section 3 develops a new approach for estimating V_{eq}/RS_{pv} based upon random vibration theory (RVT). Section 4 verifies the proposed approach by comparing with the results obtained using traditional time-series analysis. Section 5 systematically explores the influences of magnitude, distance, and site conditions on V_{eq}/RS_{pv} based on the proposed approach. Section 6 proposes a practical V_{eq}/RS_{pv} formulation that considers the influences of magnitude, distance, and site conditions. Finally, Section 7 summarizes the conclusions of the paper.

2. Current formulations for V_{eq}-RS relationship

This section reviews the existing formulations for the V_{eq}-RS relationship. Akiyama and Kitamura [28] discussed the relationship between V_{eq} and RS_v, and derived a simple formulation to relate the two spectra based on the analysis of a harmonic response, which is expressed as:

$$\frac{V_{eq}(\xi = 0.1)}{RS_v(\xi)} = \sqrt{C_{ak}} \times \sqrt{1 + 12\pi\xi} \tag{1}$$

where ξ represents the damping ratio of the SDOF oscillator. C_{ak} is an empirical coefficient obtained based on artificial and recorded seismic motions, which is expressed as:

$$\begin{gathered} C_{ak} = 1, \text{when } D_{\text{gm}} < 50s \\ C_{ak} = 1 + 0.017(D_{gm} - 50), \text{when } D_{\text{gm}} \geq 50s \end{gathered} \tag{2}$$

where D_{gm} denotes the ground motion duration. Equation (2) indicates that C_{ak} is a piecewise function related to D_{gm} with $D_{\text{gm}} = 50$ s being the demarcation point. The value of the demarcation point, i.e., 50 s, was determined based on an empirical analysis of artificial and recorded seismic motions to make Eq. (1) have good accuracy, as shown in Fig. 3 of Akiyama and Kitamura [28]. Equation (1) includes the damping ratio ξ and ground motion duration D_{gm}, which is independent of the oscillator period. This implies that V_{eq}/RS_v calculated using Eq. (1) is constant for the entire period.

Table 1
Groups of ground-motion records.

Site class	M_j	R_e (km)	Number of seismic records
B	$4 \leq M_j < 5.5$	$10 \leq R_e < 50$	551
		$50 \leq R_e < 100$	360
		$100 \leq R_e \leq 200$	98
	$5.5 \leq M_j < 6.5$	$10 \leq R_e < 50$	71
		$50 \leq R_e < 100$	149
		$100 \leq R_e \leq 200$	137
	$6.5 \leq M_j$	$10 \leq R_e < 50$	20
		$50 \leq R_e < 100$	51
		$100 \leq R_e \leq 200$	89
C	$4 \leq M_j < 5.5$	$10 \leq R_e < 50$	663
		$50 \leq R_e < 100$	489
		$100 \leq R_e \leq 200$	136
	$5.5 \leq M_j < 6.5$	$10 \leq R_e < 50$	82
		$50 \leq R_e < 100$	192
		$100 \leq R_e \leq 200$	235
	$6.5 \leq M_j$	$10 \leq R_e < 50$	51
		$50 \leq R_e < 100$	88
		$100 \leq R_e \leq 200$	206
D	$4 \leq M_j < 5.5$	$10 \leq R_e < 50$	803
		$50 \leq R_e < 100$	783
		$100 \leq R_e \leq 200$	353
	$5.5 \leq M_j < 6.5$	$10 \leq R_e < 50$	97
		$50 \leq R_e < 100$	284
		$100 \leq R_e \leq 200$	523
	$6.5 \leq M_j$	$10 \leq R_e < 50$	52
		$50 \leq R_e < 100$	58
		$100 \leq R_e \leq 200$	256
E	$4 \leq M_j < 5.5$	$10 \leq R_e < 50$	414
		$50 \leq R_e < 100$	297
		$100 \leq R_e \leq 200$	103
	$5.5 \leq M_j < 6.5$	$10 \leq R_e < 50$	62
		$50 \leq R_e < 100$	139
		$100 \leq R_e \leq 200$	271
	$6.5 \leq M_j$	$10 \leq R_e < 50$	19
		$50 \leq R_e < 100$	34
		$100 \leq R_e \leq 200$	124

Alici and Scuoglu [11] developed a formulation to relate V_{eq} to RS_{pv} based on a statistical analysis of 104 earthquakes from the NGA database, which is expressed as:

$$\frac{V_{eq}(T_0, \xi)}{RS_{pv}(T_0, \xi)} = a \times e^{-bT_0} + c \tag{3}$$

where a, b, and c are regression coefficients related to the oscillator period T_0 and damping ratio ξ presented in Table IV of Alici and Scuoglu [11]. Equation (3) is a function of T_0 and ξ.

Du et al. [26] developed a theoretical formulation for the relationship between V_{eq} and RS_{pa} according to the response analysis of a SDOF oscillator in frequency domain, which is expressed as:

$$\frac{V_{eq}(T_0, \xi)}{RS_{pa}(T_0, \xi)} = \frac{2\sqrt{\pi\xi}}{C_d\varpi} \tag{4}$$

where ϖ is the circular frequency of the SDOF oscillator ($\varpi = 2\pi/T_0$) and C_d is a parameter depending on characteristics of a specific ground motion. Du et al. [26] provided the values of C_d for four groups (shown in Fig. 6 of Du et al. [26]) classified according to the ground-motion characteristic period, T_g, defined by the ATC [27].

3. An approach for estimation of V_{eq}/RS_{pv}

To explore the influences of magnitude, distance, and site conditions on the V_{eq}-RS_{pv} relationship, an approach for estimating V_{eq}/RS_{pv} is

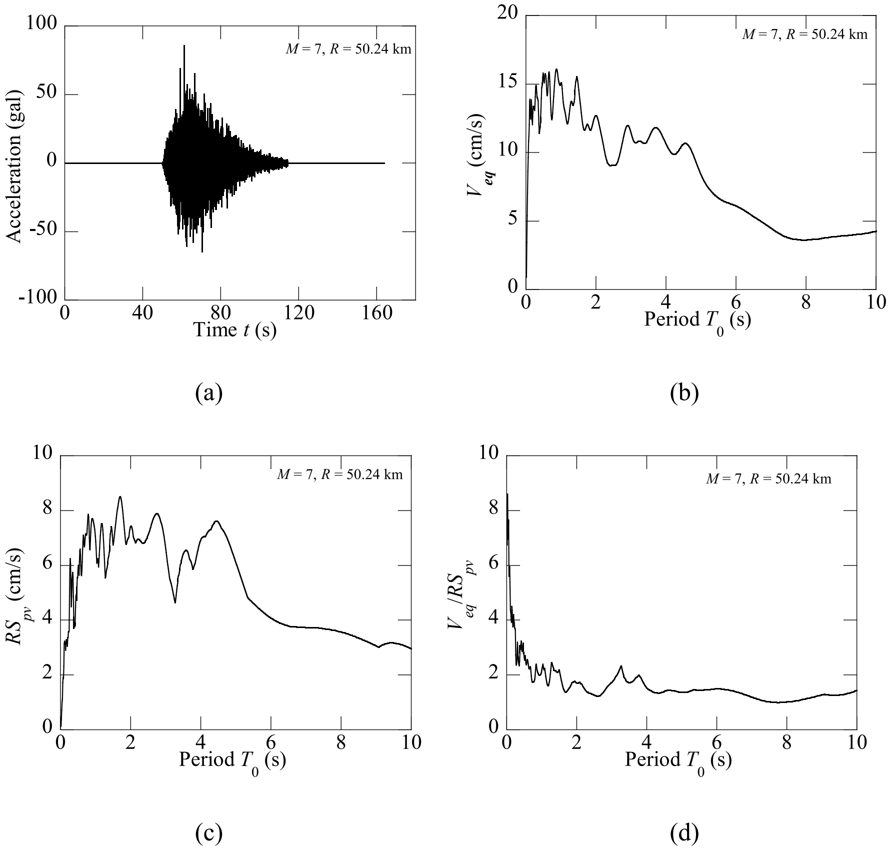

(a)

(b)

(c)

(d)

Fig. 1. Examples of (a) a generated time-series acceleration as well as the corresponding (b) energy equivalent velocity spectrum V_{eq}, (c) pseudo-velocity response spectrum RS_{pv}, and (d) V_{eq}/RS_{pv}.

developed in this section. To include magnitude, distance, and site conditions, a source-based model is desirable for characterizing the ground motion. So far, various such models for Fourier amplitude spectrum (FAS) have been developed. The simplest of them includes computing the FAS from a point source based on seismology, as introduced by Boore [30]; this FAS model, $F(f)$ (cm/s), incorporates various parameters of source, path, and site, which is expressed as:

$$F(f) = \left[0.78\frac{\pi}{\rho\beta^3}M_0\frac{f^2}{1+\left(\frac{f}{f_c}\right)^2}\right]\left[Z(R)\times\exp\left(\frac{-\pi fR}{Q(f)\beta}\right)\right]\left[\exp(-\pi\kappa_0 f)A(f)\right] \tag{5}$$

Here, f denotes the frequency (Hz); β and ρ denote the shear-wave velocity (km/s) and mass density (g/cm^3) of the crust, respectively; M_0 denotes the seismic moment (dyne-cm), which is a function of the moment magnitude M ($M_0 = 10^{1.5M+10.7}$); $\Delta\sigma$ denotes the stress drop (bar); f_c denotes the corner frequency ($f_c = 4.9\times10^6\beta(\Delta\sigma/M_0)^{1/3}$); $Z(R)$ denotes the geometric attenuation; R denotes the site-to-source distance (km); $Q(f)$ represents the anelastic attenuation; κ_0 represents the site diminution (s); and $A(f)$ represents the crust amplification. The seismological parameters required in Eq. (5) are determined according to Boore and Thompson [31], as listed in Table 1 of Wang and Rathje [32].

Then, according to FAS $F(f)$, RS_{pv} can be obtained based on the RVT [30] and can be expressed as:

$$RS_{pv}(\varpi,\xi) = pf_{p\xi}\sqrt{\frac{1}{D_{rms}\pi}\int_0^\infty|F(\omega)|^2|Hpv(\omega,\varpi,\xi)|^2d\omega} \tag{6}$$

here ω denotes the circular frequency of the FAS ($\omega = 2\pi f$), $pf_{p\xi}$ denotes the peak factor of the oscillator response, D_{rms} denotes the root-mean-square (RMS) duration of the oscillator, and $Hpv(\omega,\varpi,\xi)$ denotes the oscillator transfer function for the pseudo-velocity, which is given by

$$|Hpv(\omega,\varpi,\xi)|^2 = \frac{\varpi^2}{(2\xi\omega\varpi)^2+(\omega^2-\varpi^2)^2} \tag{7}$$

To obtain RS_{pv} using Eq. (6), the peak factor needs to be calculated. Some formulations for the peak factor (pf) have been proposed [33–35]. Several studies [31,32] found that the formulation by Vanmarcke [35] provided the best estimates of the response spectra in the RVT analysis. The cumulative distribution function (CDF), P, of pf for the Vanmarcke formulation [35], is given by:

$$P(pf<r) = [1-e^{(-r^2/2)}]\times\exp[-2f_z\exp(-r^2/2)D_{gm}\frac{(1-e^{-\delta^{1.2}r\sqrt{\pi/2}})}{(1-e^{r^2/2})}] \tag{8}$$

In Eq. (8), δ is a bandwidth factor, which is expressed as:

$$\delta = \sqrt{1-\frac{m_1^2}{m_0m_2}} \tag{9}$$

where m_0, m_1, and m_2 are the zeroth-order, first-order, and second-order moments of the square of the FAS, respectively; the nth-order spectral moment, m_n, for a FAS, $y(\omega)$, is expressed as:

$$m_n = \frac{1}{\pi}\int_0^\infty\omega^n|y(\omega)|^2d\omega \tag{10}$$

When calculating the oscillator response peak factor pf_ξ using Eq. (8), the oscillator-response FAS should be utilized in Eq. (10). In Eq. (8), f_z represents the zero crossings rate, and is also related to the spectral moments, which is expressed as:

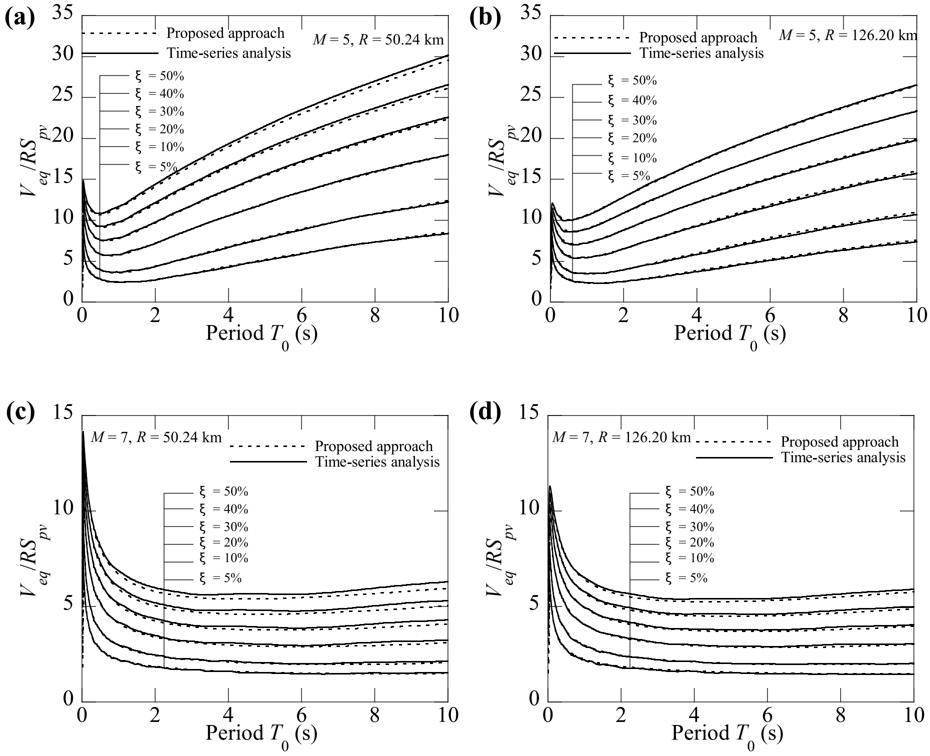

Fig. 2. Comparison of the average V_{eq}/RS_{pv} values obtained using the time-series analysis and proposed approach considering different damping ratios for various values of moment magnitude M and distance R: (a) $M = 5$, $R = 50.24$ km; (b) $M = 5$, $R = 126.20$ km; (c) $M = 7$, $R = 50.24$ km; and (d) $M = 7$, $R = 126.20$ km.

$$f_z = \frac{1}{2\pi}\sqrt{\frac{m_2}{m_0}} \tag{11}$$

When calculating the mean value of RS_{pv} using Eq. (6), the mean value of the peak factor $pf_{p\xi}$ should be utilized, which can be calculated by Eq. (8) using the equation $\int_0^\infty [1 - P(pf < r)]dr$. When estimating the

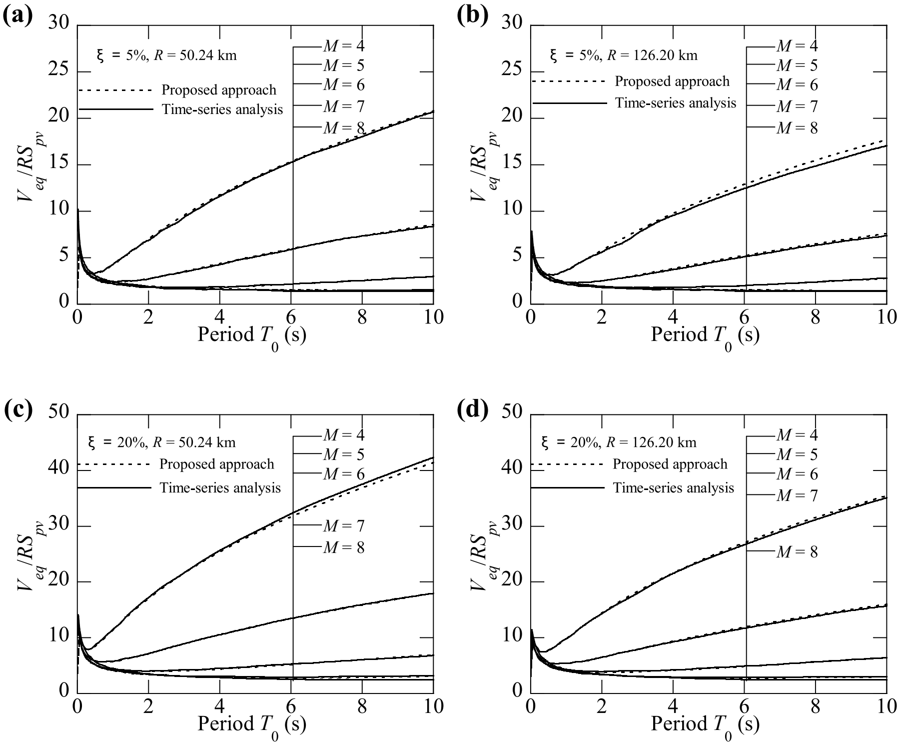

Fig. 3. Comparison of the average V_{eq}/RS_{pv} values obtained using the time-series analysis and proposed approach considering different moment magnitudes for various values of the damping ratio ξ and distance R: (a) $\xi = 5$ %, $R = 50.24$ km; (b) $\xi = 5$ %, $R = 126.20$ km; (c) $\xi = 20$ %, $R = 50.24$ km; and (d) $\xi = 20$ %, $R = 126.20$ km.

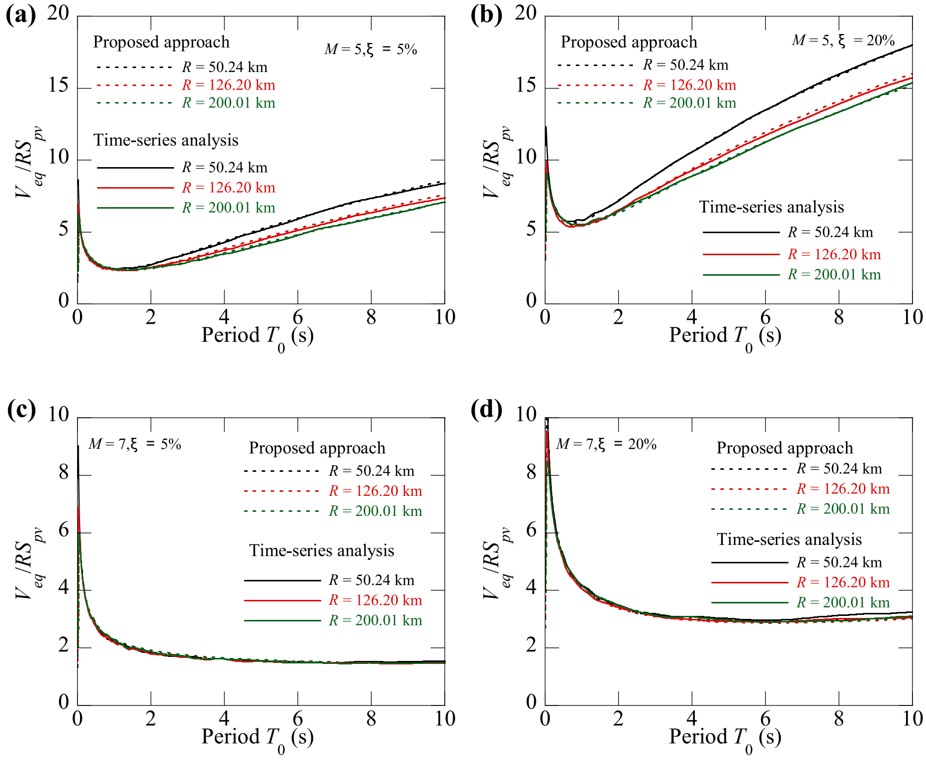

Fig. 4. Comparison of the average V_{eq}/RS_{pv} values obtained using the time-series analysis and proposed approach considering different distances for various values of the moment magnitude M and damping ratio ξ: (a) $M = 5$, $\xi = 5$ %; (b) $M = 5$, $\xi = 20$ %; (c) $M = 7$, $\xi = 5$ %; and (d) $M = 7$, $\xi = 20$ %.

variation of RS_{pv} using Eq. (6), the probability distribution of the peak factor $pf_{p\xi}$ should be considered according to its CDF expressed by Eq. (8), although this has rarely been performed.

The ground motion duration, D_{gm}, is utilized in Eq. (8) for the estimation of $pf_{p\xi}$ [36], and can be determined using the model of Boore and Thompson [31,37]. The RMS duration of the oscillator, D_{rms}, in Eq. (6) is related to the ground motion duration D_{gm} [31,36,38,39]. The latest model for D_{rms}/D_{gm} by Boore and Thompson [31] was used in this

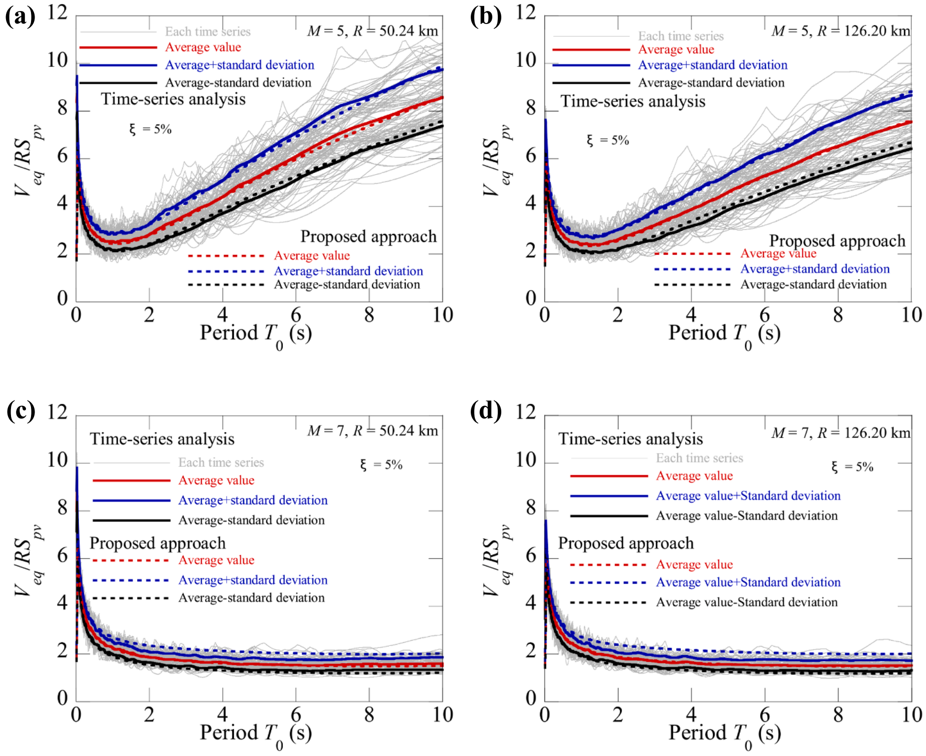

Fig. 5. Comparison of mean ± standard deviation values of V_{eq}/RS_{pv} obtained from the time-series analysis and proposed approach considering different values of moment magnitude M and distance R: (a) $M = 5$, $R = 50.24$ km; (b) $M = 5$, $R = 126.20$ km; (c) $M = 7$, $R = 50.24$ km; and (d) $M = 7$, $R = 126.20$ km.

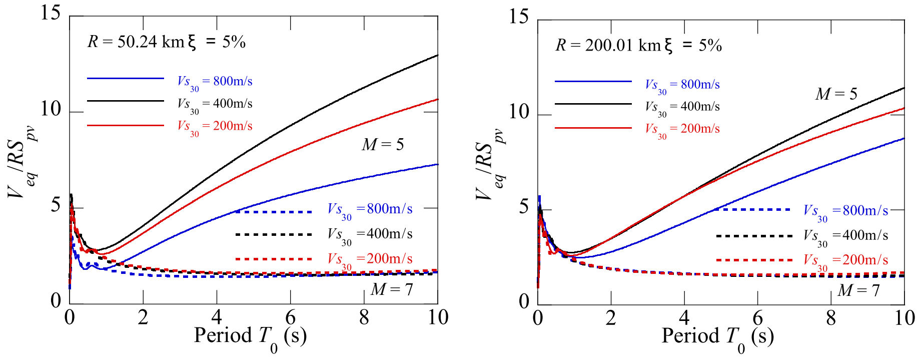

(a)

(b)

Fig. 6. Effects of site conditions on V_{eq}/RS_{pv} for different values of distance R: (a) $R = 50.24$ km and (b) $R = 200.01$ km.

study and is expressed as:

$$\frac{D_{rms}}{D_{gm}} = \left(c_{e1} + c_{e2}\frac{1-\eta^{c_{e3}}}{1+\eta^{c_{e3}}}\right)\left[1 + \frac{c_{e4}}{2\pi\xi}\left(\frac{\eta}{1+c_{e5}\eta^{c_{e6}}}\right)^{c_{e7}}\right] \tag{12}$$

where $\eta = T_0/D_{gm}$, and c_{e1}–c_{e7} are coefficients depending on the distance R and moment magnitude M, as given by Boore and Thompson [31].

In addition, the theoretical relationship between the input energy spectrum E_I and FAS of the ground motion has been derived as [40]:

$$V_{eq}(\varpi,\xi) = \sqrt{\frac{2E_I(\varpi,\xi)}{m}} = \sqrt{-\frac{2}{\pi}\int_0^{\infty}|F(\omega)|^2 Re[Hv(\varpi,\omega,\xi)]d\omega} \tag{13}$$

where $Hv(\varpi,\omega,\xi)$ denotes the oscillator transfer function of the ground acceleration to the relative velocity, which is a complex number; its real part is expressed as:

$$Re[Hv(\varpi,\omega,\xi)] = -\frac{2\xi\varpi\omega^2}{(\varpi^2-\omega^2)^2 + (2\xi\omega\varpi)^2} \tag{14}$$

Thus, based on Eqs. (6) and (13), V_{eq}/RS_{pv} can be obtained as follows:

$$\frac{V_{eq}(\varpi,\xi)}{RS_{pv}(\varpi,\xi)} = \sqrt{\frac{\int_0^{\infty}|F(\omega)|^2(-Re[Hv(\varpi,\omega,\xi)])d\omega}{\int_0^{\infty}|F(\omega)|^2|Hpv(\omega,\varpi,\xi)|^2 d\omega}} \times \frac{\sqrt{2D_{rms}}}{pf_{p\xi}} \tag{15}$$

Equation (15) relates V_{eq} and RS_{pv}, and includes the magnitude M, distance R, and site conditions; thus, it is suitable for the exploration of the influences of these parameters on V_{eq}/RS_{pv}.

4. Verification of the proposed approach

To confirm the accuracy of the proposed approach in the previous section, the V_{eq}/RS_{pv} values were calculated using Eq. (15) and compared with those calculated based on traditional time-series analysis. To this end, a wide range of oscillator periods T_0 (0.01–10 s), damping ratios ξ (5 %–50 %), distance R (50.24–200.01 km), and moment magnitude M (4–8) were considered. Since a point source model may be inappropriate for cases with very short distances but large magnitudes, the selection of the distance and magnitude ranges also considers this limitation. The reason for using very accurate distances, e.g., 50.24 km and 200.01 km, is that the coefficients c_{e1}–c_{e7} in Eq. (12) were given in tabular form corresponding to these accurate discrete distances, by Boore and Thompson (2015). To avoid interpolation, the distances for which these coefficients can be directly obtained are used. For each FAS obtained using Eq. (5) and considering a pair of M and R, 100 time-series accelerations were generated using SMSIM [41]. Then, the V_{eq}/RS_{pv} values for the generated accelerations were computed based on the direct integration method [42]. Examples of a generated time-series acceleration, as well as the corresponding V_{eq}, RS_{pv}, and V_{eq}/RS_{pv} are shown in Fig. 1. Then, the average values of V_{eq}/RS_{pv} from the 100 time-series accelerations were calculated and compared with those calculated by Eq. (15), as shown in Figs. 2–4. In addition, the mean ± standard deviation values of V_{eq}/RS_{pv}, which represent the variations of V_{eq}/RS_{pv}, are presented in Fig. 5. It is noted from Figs. 2–4 that the average V_{eq}/RS_{pv} values obtained using the proposed approach agree very well with those acquired from the time-series analysis. Fig. 5 indicates that, although the mean ± standard deviation values by the proposed approach deviated slightly from those of the time-series analysis for cases with large magnitudes (Fig. 5(c) and (d)), the average relative error from 0.01 s to 10 s is limited to 15 %.

Figs. 2–5 also show that the values of V_{eq}/RS_{pv} are typically larger than unity for most oscillator periods, which means that V_{eq} is generally larger than RS_{pv}. In addition, Fig. 2 indicates that V_{eq}/RS_{pv} increases with an increasing damping ratio ξ. This is because RS_{pv} decreases with an increasing damping ratio ξ, whereas V_{eq} is insensitive to the damping ratio ξ [28]. These phenomena are consistent with those observed in previous studies [11,26], which further supports the rationality of the proposed approach.

5. Influences of magnitude, distance and site conditions on V_{eq}/RS_{pv}

The influences of the moment magnitude M and distance R on the V_{eq}-RS_{pv} relationship can be clearly observed in Figs. 2–4. Figs. 2 and 3 indicate that V_{eq}/RS_{pv} varies significantly with the moment magnitude M for long oscillator periods ($T_0 \gtrsim 1$ s) and decreases with an increasing M. This means that the values of V_{eq} approach those of RS_{pv} with an increasing moment magnitude M. The shape of V_{eq}/RS_{pv} flattens with an increase in the moment magnitude M (Fig. 3), which means that the shape of V_{eq} also becomes similar to that of RS_{pv}. In addition, Fig. 3 indicates that when the moment magnitude M increases from 4 to 6, V_{eq}/RS_{pv} decreases significantly for long oscillator periods; additionally, when M further increases to 8, the change of V_{eq}/RS_{pv} becomes smaller. This means that V_{eq}/RS_{pv} is very sensitive to the moment magnitude M when M has a small-to-moderate value, whereas as the moment magnitude M increases, V_{eq}/RS_{pv} becomes not that sensitive to it. Fig. 4 indicates that when the moment magnitude M is moderate (Fig. 4(a) and 4(b)), V_{eq}/RS_{pv} varies with the distance R; when the moment magnitude M is large (Fig. 4(c) and 4(d)), the change in V_{eq}/RS_{pv} with distance R is quite small. In addition, the variation of V_{eq}/RS_{pv} with the distance R is irregular for the cases with a moderate moment magnitude M. Moreover, Fig. 5 shows that the standard deviation of V_{eq}/RS_{pv} (i.e., the dispersions) decreases with increasing moment magnitude M and is not that sensitive to the distance R.

To explore the influences of site conditions on the V_{eq}-RS_{pv}

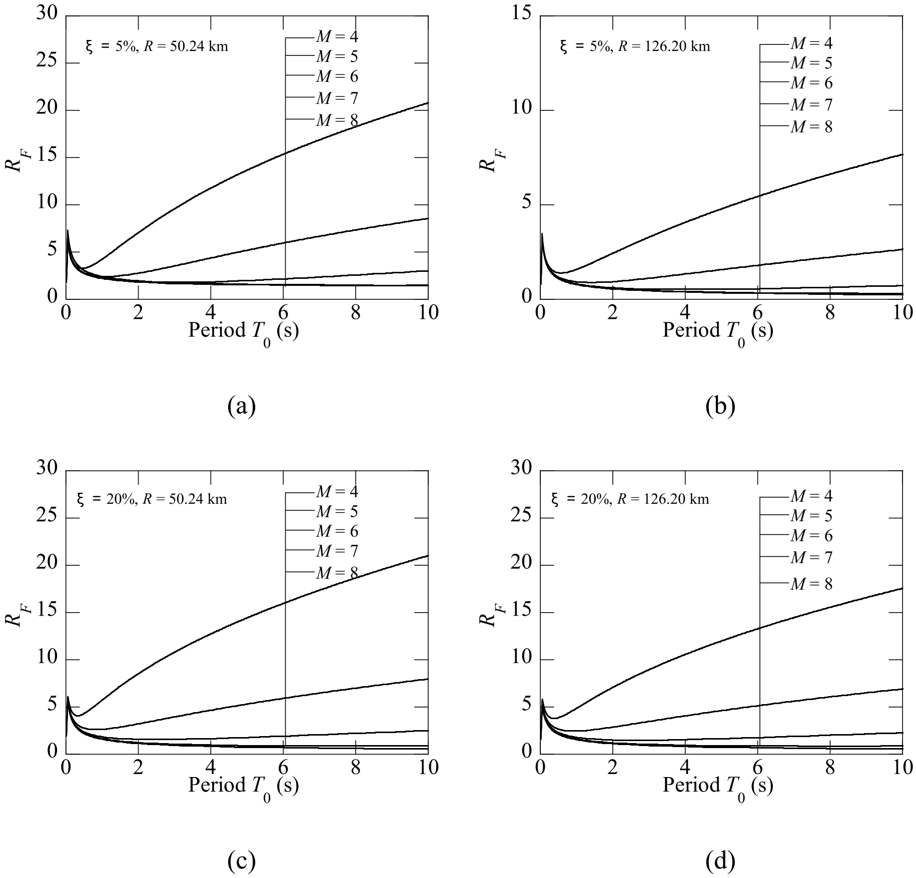

Fig. 7. Values of the first part, R_F, of Eq. (15) for different values of damping ratio ξ and site-to-source distance R: (a) $\xi = 5$ %, $R = 50.24$ km; (b) $\xi = 5$ %, $R = 126.20$ km; (c) $\xi = 20$ %, $R = 50.24$ km; and (d) $\xi = 20$ %, $R = 126.20$ km.

relationship, three single-layer soil sites belonging to different soil types defined in the National Earthquake Hazards Reduction Program (NEHRP) [43] were considered. The average shear-wave velocities in the upper 30 m, Vs_{30}, for the three soil sites are 800 m/s (site class B), 400 m/s (site class C), and 200 m/s (site class E). The heights of the three soil sites are all considered as 30 m. The FAS of the rock site obtained using Eq. (5) was propagated through the three soil sites. The V_{eq}/RS_{pv} values for the three soil sites were obtained from the FAS on the soil sites using Eq. (15), as shown in Fig. 6. It is noted that similar to the influence of the distance R on V_{eq}/RS_{pv}, the site conditions affect V_{eq}/RS_{pv} for the cases with moderate moment magnitude M; also, the influences of site conditions on V_{eq}/RS_{pv} are quite small for the cases with large moment magnitude M. In addition, the change in V_{eq}/RS_{pv} with site conditions is irregular for the cases with moderate magnitude M.

To further investigate the main parameter - i.e., the moment magnitude M - affecting V_{eq}/RS_{pv}, the derived equation (Eq. (15)) was analyzed in detail. It can be found from Eq. (15) that the moment magnitude M affects V_{eq}/RS_{pv} essentially by changing two factors: the FAS $F(\omega)$ and ground-motion duration D_{gm}. To investigate the impact of each factor on V_{eq}/RS_{pv}, Eq. (15) is divided into two parts: the first part R_F, i.e.,$\sqrt{\frac{\int_0^\infty |F(\omega)|^2(-Re[Hv(\varpi,\omega,\xi)])d\omega}{\int_0^\infty |F(\omega)|^2|Hpv(\omega,\varpi,\xi)|^2 d\omega}}$), and the second part R_S, i.e., $\frac{\sqrt{2D_{rms}}}{pf_{p\xi}}$. The FAS $F(\omega)$ influences the first part ($\sqrt{\frac{\int_0^\infty |F(\omega)|^2(-Re[Hv(\varpi,\omega,\xi)])d\omega}{\int_0^\infty |F(\omega)|^2|Hpv(\omega,\varpi,\xi)|^2 d\omega}}$) as well as the peak factor $pf_{p\xi}$ (Eq. (8)); and the ground-motion duration D_{gm} influences the second part R_S ($\frac{\sqrt{2D_{rms}}}{pf_{p\xi}}$) by changing the peak factor $pf_{p\xi}$ (Eq. (8)) and RMS duration D_{rms} (Eq. (12)). The R_F and R_S results corresponding to the cases shown in Fig. 3 are presented in Figs. 7 and 8, respectively. The coordinates of Figs. 7 and 8 are unified for the convenience of comparing the R_F and R_S results. Figs. 3 and 7 indicate that R_F and V_{eq}/RS_{pv} have the same variation trend as the moment magnitude M, and the shape of R_F is similar to that of V_{eq}/RS_{pv}. In addition, Fig. 8 shows that the variation in R_S with the moment magnitude M is much smaller than the variation in R_F, and the shape of R_S is much flatter. These results indicate that the influence of the moment magnitude is dominated by the first part R_F, and the contribution of the second part R_S is small. Therefore, it can be inferred that the moment magnitude affects V_{eq}/RS_{pv} mainly by changing the FAS instead of the ground-motion duration D_{gm}. A schematic illustrating how the moment magnitude M affects V_{eq}/RS_{pv} is depicted in Fig. 9. Furthermore, it is observed from Eq. (15) that FAS's distribution with period/frequency instead of FAS's values influences the first part R_F. This point can be supported by multiplying the FAS by a constant value; because this value will exist in both the numerator and denominator of R_F, it cancels and will not influence R_F. Therefore, the key factor controlling the influence of moment magnitude is the FAS's distribution with frequency, i.e., the frequency content of the ground motion.

To clarify how the ground motion frequency content affects V_{eq}/RS_{pv}, the first part R_F was explored. After comparing the numerator and denominator of R_F, it is found that only the two terms related to the oscillator transfer functions – i.e., $(-Re[Hv(\varpi,\omega,\xi)])$ and $|Hpv(\omega,\varpi,\xi)|^2$ - are different. The values of $(-Re[Hv(\varpi,\omega,\xi)])$ and $|Hpv(\omega,\varpi,\xi)|^2$ for $f_0 = 1$ Hz ($f_0 = 1/T_0$) and $\xi = 5$ % are compared in Fig. 10. It can be observed that$(-Re[Hv(\varpi,\omega,\xi)]) < |Hpv(\omega,\varpi,\xi)|^2$at low frequencies and$(-Re[Hv(\varpi,\omega,\xi)]) > |Hpv(\omega,\varpi,\xi)|^2$ at high frequencies. It can be derived from Eq. (7) and (14) that when $\omega = \sqrt{\varpi/2\xi}$, $(-Re[Hv(\varpi,\omega,\xi)])=|Hpv(\omega,\varpi,\xi)|^2$. Therefore, it can be concluded that when $\omega < \sqrt{\varpi/2\xi}$, $|F(\omega)|^2(-Re[Hv(\varpi,\omega,\xi)])<|F(\omega)|^2|Hpv(\omega,\varpi,\xi)|^2$; and when $\omega > \sqrt{\varpi/2\xi}$, $|F(\omega)|^2(-Re[Hv(\varpi,\omega,\xi)]) > |F(\omega)|^2|Hpv(\omega,\varpi,\xi)|^2$. The

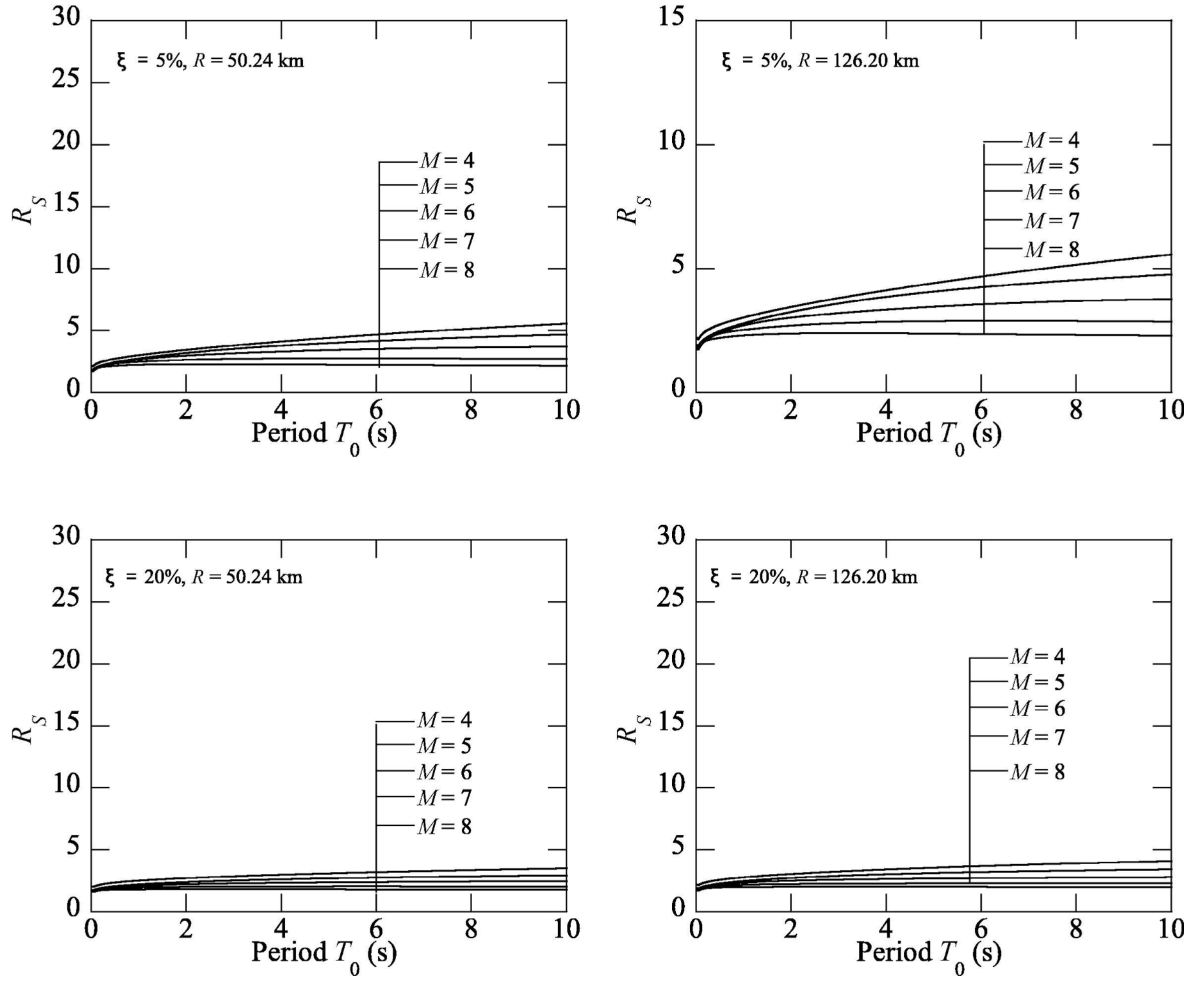

Fig. 8. Values of the second part, R_S, of Eq. (15) for different values of damping ratio ξ and distance R: (a) $\xi = 5$ %, $R = 50.24$ km; (b) $\xi = 5$ %, $R = 126.20$ km; (c) $\xi = 20$ %, $R = 50.24$ km; and (d) $\xi = 20$ %, $R = 126.20$ km.

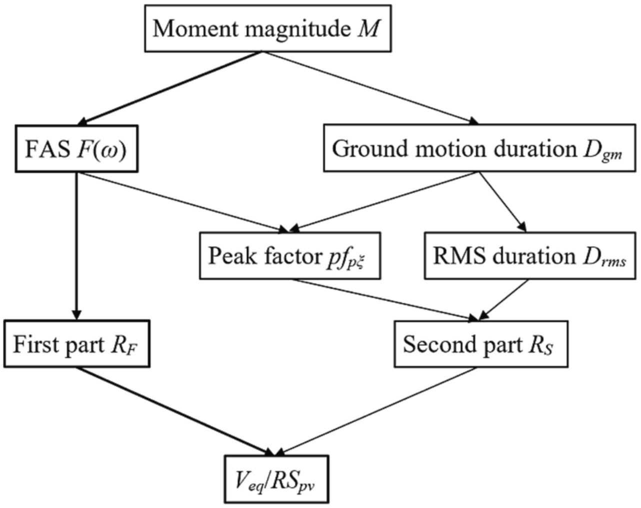

Fig. 9. Schematic illustrating how the moment magnitude M affects V_{eq}/RS_{pv}.

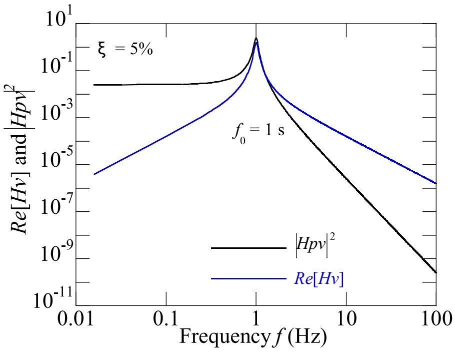

Fig. 10. Comparison of two terms related to the oscillator transfer functions $(-Re[Hv(\varpi, \omega, \xi)])$ and $|Hpv(\omega, \varpi, \xi)|^2$.

results of $|F(\omega)|^2(-Re[Hv(\varpi, \omega, \xi)])$ and $|F(\omega)|^2|Hpv(\omega, \varpi, \xi)|^2$ for the two cases with $M = 5$ and $M = 7$ are shown in Fig. 11(a) and 11(b), respectively. To easily understand the effect of the ground-motion frequency content on the first term R_F, $\int_0^\infty |F(\omega)|^2(-Re[Hv(\varpi, \omega, \xi)])d\omega$ and $\int_0^\infty |F(\omega)|^2|Hpv(\omega, \varpi, \xi)|^2 d\omega$ are divided into left and right parts with $\omega = \sqrt{\varpi/2\xi}$ as the dividing line, respectively. Thus, the first part R_F can be rewritten as:

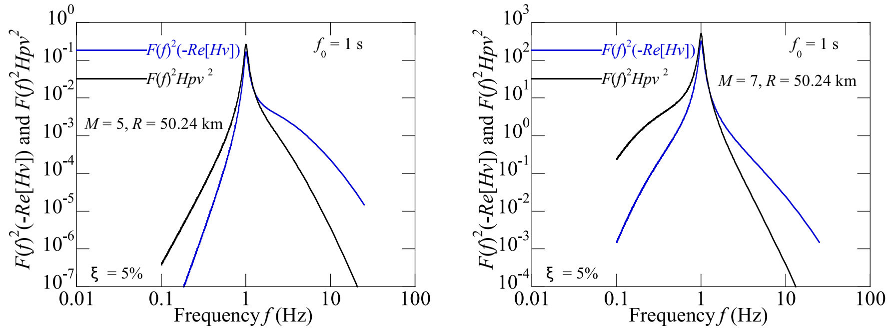

(a)

(b)

Fig. 11. Comparison of $|F(\omega)|^2(-Re[Hv(\overline{\omega},\omega,\xi)])$ and $|F(\omega)|^2|Hpv(\omega,\overline{\omega},\xi)|^2$ for different values of moment magnitude M: (a) $M = 5$ and (b) $M = 7$.

$$R_F = \sqrt{\frac{\int_0^{\sqrt{\overline{\omega}/2\xi}}|F(\omega)|^2(-Re[Hv(\overline{\omega},\omega,\xi)])d\omega + \int_{\sqrt{\overline{\omega}/2\xi}}^{\infty}|F(\omega)|^2(-Re[Hv(\overline{\omega},\omega,\xi)])d\omega}{\int_0^{\sqrt{\overline{\omega}/2\xi}}|F(\omega)|^2|Hpv(\omega,\overline{\omega},\xi)|^2d\omega + \int_{\sqrt{\overline{\omega}/2\xi}}^{\infty}|F(\omega)|^2|Hpv(\omega,\overline{\omega},\xi)|^2d\omega}} = \sqrt{\frac{SE_l + SE_r}{SV_l + SV_r}} \tag{16}$$

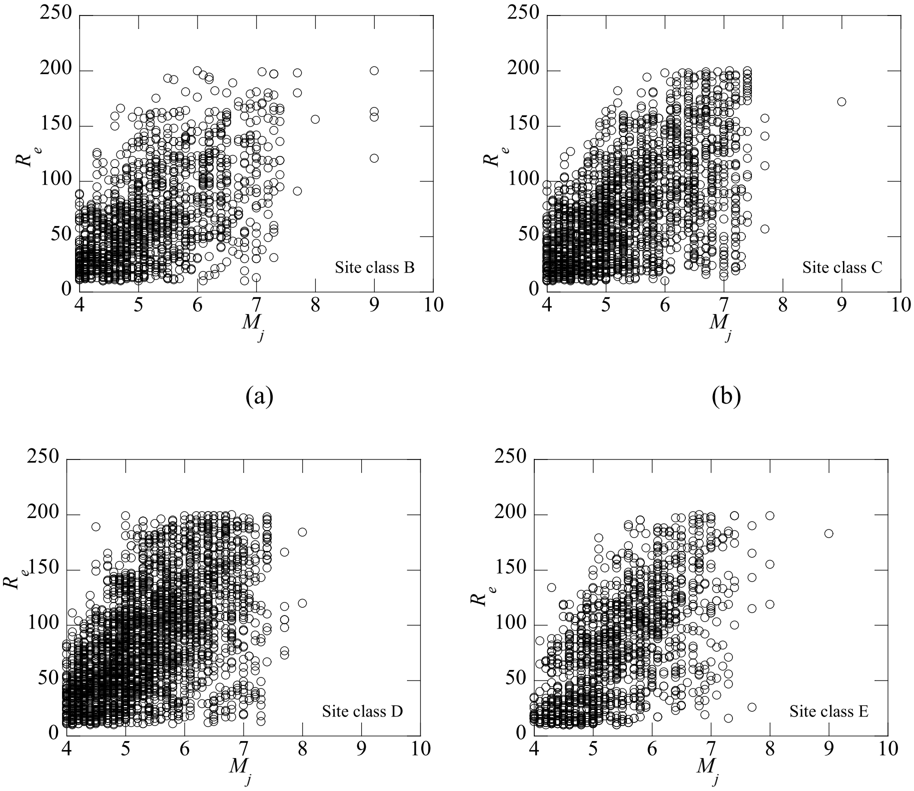

(a)

(b)

(c)

(d)

Fig. 12. Distribution of Japan Meteorological Agency magnitude M_j and epicentral distance R_e of ground motions used in this paper for site classes: (a) B, (b) C, (c) D, and (d) E.

Table 2
Coefficients of Eq. (18).

Site class	ζ	C_{z1}	C_{z2}	C_{z3}
B	0.00124	−0.0247	0.4263	1.6208
	0.00125	−0.0417	0.8216	1.5629
	0.00140	−0.0682	1.2373	1.6478
	0.00545	0.0139	−0.1055	1.8520
	0.00652	0.0135	−0.0752	2.1277
	0.00706	−0.0038	0.1275	2.1644
	0.01707	0.0197	−0.2198	2.1063
	0.02137	0.0125	−0.1883	2.3195
	0.02446	0.0208	−0.2960	2.7388
C	0.00150	−0.0145	0.4260	1.6160
	0.00168	−0.0333	0.6611	1.6631
	0.00188	−0.0411	0.9357	1.6940
	0.00892	0.0175	−0.1219	1.8488
	0.00901	0.0111	−0.0542	2.1139
	0.00949	0.0043	0.0244	2.2738
	0.02660	0.0184	−0.2227	2.2335
	0.03147	0.0148	−0.2085	2.3005
	0.03734	0.0182	−0.2334	2.5349
D	0.00263	−0.0121	0.5061	1.6321
	0.00279	−0.0234	0.6607	1.7761
	0.00284	−0.0188	0.7882	1.9481
	0.01101	0.0115	−0.0169	1.8766
	0.01180	0.0100	0.0002	2.2484
	0.01292	0.0157	0.0297	2.3949
	0.04351	0.0172	−0.2156	2.0899
	0.05265	0.0136	−0.1809	2.4184
	0.05435	0.0048	−0.1289	2.5049
E	0.00568	−0.0077	0.3026	1.7248
	0.00598	−0.0120	0.4584	1.7581
	0.00633	−0.0023	0.4976	1.7292
	0.02043	0.0035	0.0585	1.9249
	0.02073	0.0138	0.0064	2.2283
	0.02356	0.0100	0.0720	2.2627
	0.04454	0.0058	−0.0347	1.8830
	0.08372	0.0025	−0.0575	2.1935
	0.08597	0.0084	−0.1124	2.4950

It is clear that $\int_0^{\sqrt{\overline{\omega}/2\xi}}|F(\omega)|^2(-Re[Hv(\overline{\omega},\omega,\xi)])d\omega$ (SE_l) $<\int_0^{\sqrt{\overline{\omega}/2\xi}}|F(\omega)|^2|Hpv(\omega,\overline{\omega},\xi)|^2d\omega$ (SV_l) and $\int_{\sqrt{\overline{\omega}/2\xi}}^{\infty}|F(\omega)|^2(-Re[Hv(\overline{\omega},\omega,\xi)])d\omega(SE_r)>\int_{\sqrt{\overline{\omega}/2\xi}}^{\infty}|F(\omega)|^2|Hpv(\omega,\overline{\omega},\xi)|^2d\omega(SV_r)$. Equation (16) shows that when the low-frequency components of $F(\omega)$ increase relative to the high-frequency components, the left parts (i.e., SE_l and SV_l) increase relative to the right parts (i.e., SE_r and SV_r); thus, $\frac{SE_l+SE_r}{SV_l+SV_r}$ approaches $\frac{SE_l}{SV_l}$ ($\frac{SE_l}{SV_l}<1$). In contrast, when the high-frequency components of $F(\omega)$ increase relative to the low-frequency components, the right parts, (i.e., SE_r and SV_r) increase relative to the left parts, (i.e., SE_l and SV_l); thus, $\frac{SE_l+SE_r}{SV_l+SV_r}$ approaches $\frac{SE_r}{SV_r}$ ($\frac{SE_r}{SV_r}>1$). Therefore, the first part R_F decreases (approaches $\sqrt{\frac{SE_l}{SV_l}}$) with increasing low-frequency components of $F(\omega)$. It is well known that the low-frequency components of $F(\omega)$ increase relatively with increasing moment magnitude M. In addition, the effect of the magnitude on V_{eq}/RS_{pv} is dominated by the first part R_F. Hence, V_{eq}/RS_{pv} decreases with increase in the low-frequency components of $F(\omega)$ and moment magnitude M.

6. A practical V_{eq}/RS_{pv} formulation

Section 5 indicates that V_{eq}/RS_{pv} is affected significantly by the magnitude (Fig. 3) and moderately by distance and site conditions for cases with moderate magnitude (Figs. 4 and 6). In principle, all of these parameters should be incorporated into the V_{eq}/RS_{pv} formulation. However, the magnitude and distance are typically not given out in seismic codes. It was found that the magnitude affected V_{eq}/RS_{pv} by changing the frequency content of the ground motion. Hence, a factor representing the ground motion frequency content is used to reflect their effects. Zhang and Zhao [44] developed a factor to quantify the ground motion frequency content, which is expressed as:

$$\zeta=\frac{RS_{pa}(6s)}{PGA} \tag{17}$$

where RS_{pa}(6 s) is the pseudo-spectral acceleration at 6 s, and peak ground acceleration (PGA) equals the pseudo-spectral acceleration at 0 s. It can be noted that the simple factor ζ can be easily computed using RS_{pa} in seismic codes. In addition, Zhang and Zhao [44] proved that ζ is closely correlated with magnitude and distance, and can reasonably represent the ground motion frequency content.

To establish a practical V_{eq}/RS_{pv} formulation, 16,660 real seismic records were collected from the strong-motion seismograph networks (K-net, Kik-net) of Japan [45]. To ensure a sufficient signal-to-noise ratio, all the seismic records were selected with PGA being larger than 20 Gal. The Japan Meteorological Agency (JMA) magnitude M_j of the ground motions varies from 4 to 9, and the epicentral distance R_e varies from 10 km to 200 km, as shown in Fig. 12. The selected earthquakes include both interplate (e.g., 2003 Tokachi earthquake and 2011 off the Pacific coast of Tohoku earthquake) and intraplate earthquakes (e.g., 2000 Tottori earthquake, 2004 Chūetsu earthquake, 2016 Kumamoto earthquakes, and 2018 Hokkaido Eastern Iburi earthquake). In this study, the JMA magnitude M_j and epicentral distance R_e were used instead of the moment magnitude and rupture distance, because K-NET and KiK-net only provide information on M_j and R_e. These seismic records were recorded at 338 stations in Japan, covering the four site classes defined by NEHRP [43]. Among these stations, 63 stations belong to site class B, 112 stations belong to site class C, 107 stations belong to site class D, and 56 stations belong to site class E. For the K-NET stations, because only the soil data in the upper 20 m were provided, Vs_{30} used for site classification was obtained from the average shear-wave velocity in the upper 20 m (Vs_{20}) using the correlation equation of Kanno et al. [46]. These seismic records were used in our previous study [44].

Then, a practical V_{eq}/RS_{pv} formulation was proposed based on a statistical analysis of the selected seismic records. To obtain smooth V_{eq}/RS_{pv} results, the selected seismic records were classified into 45 groups according to the JMA magnitude M_j, epicentral distance R_e, and site conditions listed in Table 1. A large number of function forms are trialed to fit the average values of V_{eq}/RS_{pv} in each group. Then, considering a balance between accuracy and simplicity, an equation for V_{eq}/RS_{pv} was regressed as:

$$\frac{V_{eq}(T_0,5\%)}{RS_{pv}(T_0,5\%)}=C_{z1}T_0^2+C_{z2}T_0+C_{z3} \tag{18}$$

where $C_{z1}-C_{z3}$ are the regression coefficients that depend on the frequency-content factor ζ and site conditions, as listed in Table 2. Since V_{eq}/RS_{pv} is moderately affected by site conditions for cases with moderate magnitudes, the coefficients $C_{z1}-C_{z3}$ are regressed as functions of the site class for such cases. Although the effect of site conditions becomes very small for cases with large magnitudes, for consistency, the same regression process is implemented. More importantly, this can avoid determining criteria to judge if site conditions should be considered and avoid giving different tables for different cases, which makes the proposed formulation more convenient.

It can be observed from Figs. 13–15 that the results of V_{eq}/RS_{pv} calculated by the proposed formulation agree very well with the results of the actual seismic records for most oscillator periods. The accuracy of the proposed formulation is not that good at very short periods ($\lesssim$0.15), which can be improved by increasing regression coefficients in principle. However, since V_{eq}/RS_{pv} varies greatly with the oscillator period T_0 at very short periods, a small increase in accuracy needs increasing many regression coefficients, which will lead to a very complicated formulation. Considering a balance between accuracy and simplicity, Eq. (18) is considered to be ideal. In addition, the accuracy of the proposed formulation was found to be better than those of previous formulations (Fig. 13(a)). The V_{eq}/RS_{pv} results of Alici and Scuoglu [11] and Du et al.

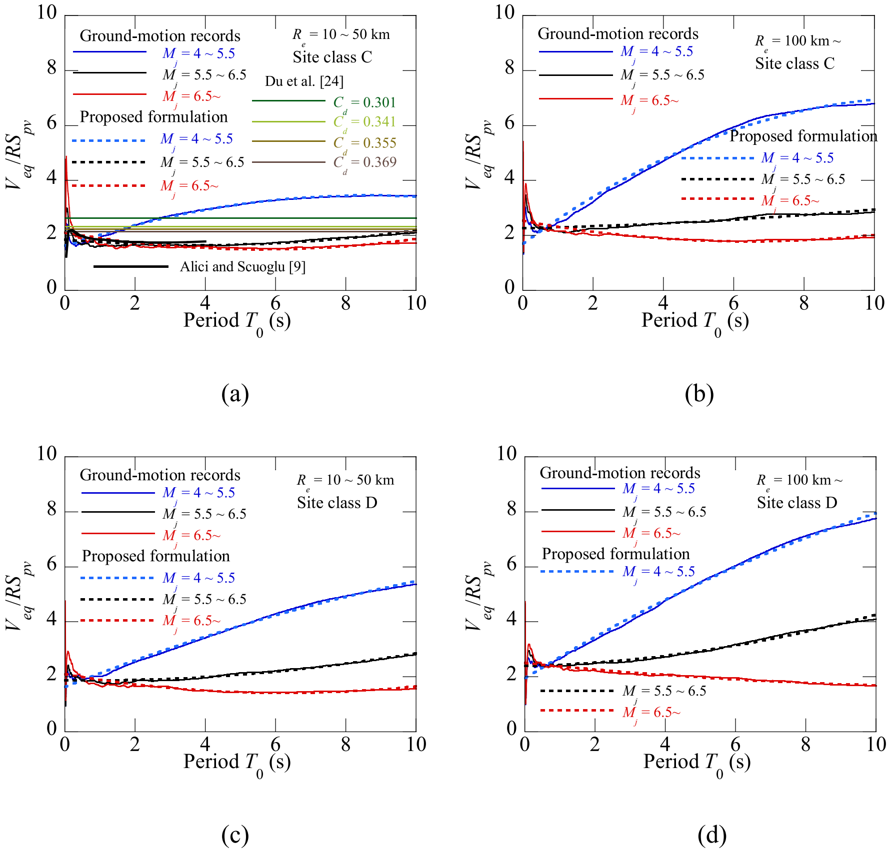

Fig. 13. Comparisons of the average V_{eq}/RS_{pv} values obtained from seismic records and Eq. (18) for different cases of soil type and distance: (a) Site class C, R_e = 10–50 km; (b) Site class C, R_e = 100 km ~; (c) Site class D, R_e = 10–50 km; and (d) Site class D, R_e = 100 km ~.

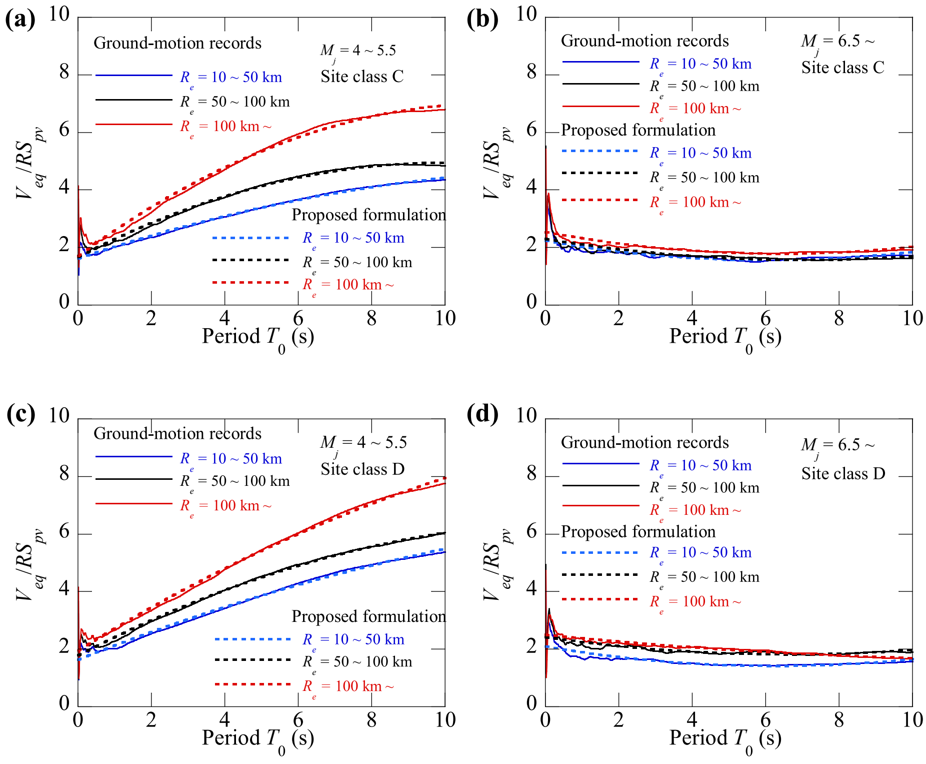

Fig. 14. Comparisons of the average V_{eq}/RS_{pv} values obtained from seismic records and Eq. (18) for different cases of soil type and magnitude: (a) Site class C, M_j = 4–5.5; (b) Site class C, M_j = 6.5 ~; (c) Site class D, M_j = 4–5.5; and (d) Site class D, M_j = 6.5 ~.

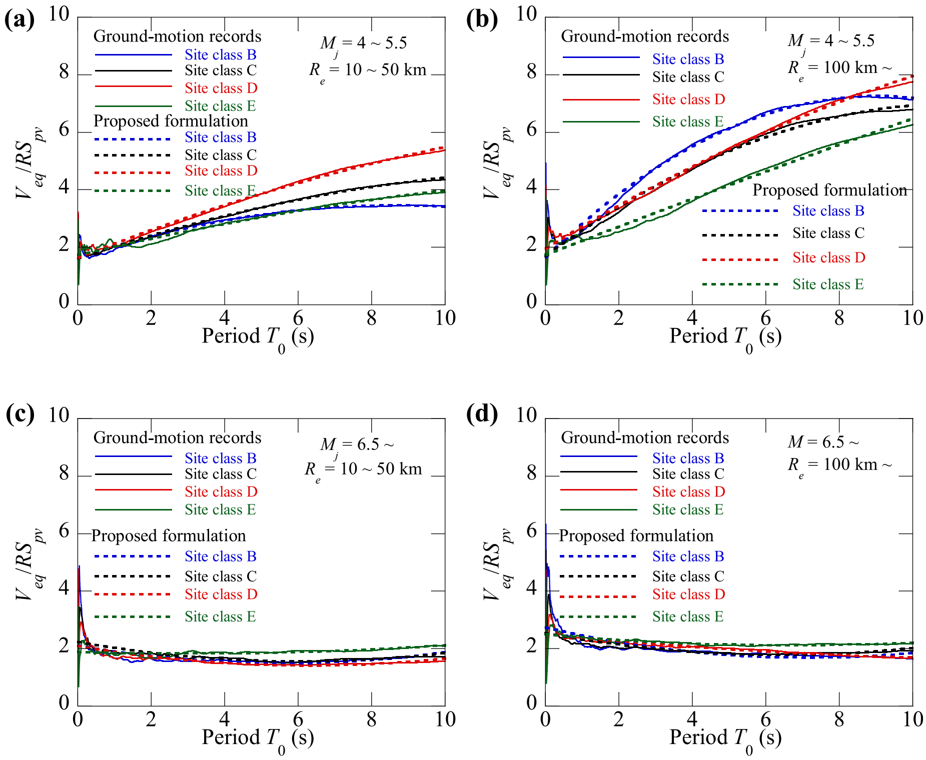

Fig. 15. Comparisons of the average V_{eq}/RS_{pv} values obtained from seismic records and Eq. (18) for different cases of magnitude and distance: (a) $M_j = 4$–5.5, $R_e =$ 10–50 km; (b) $M_j = 4$–5.5, $R_e = 100$ km ~; (c) $M_j = 6.5$ ~, $R_e = 10$–50 km; and (d) $M_j = 6.5$ ~, $R_e = 100$ km ~.

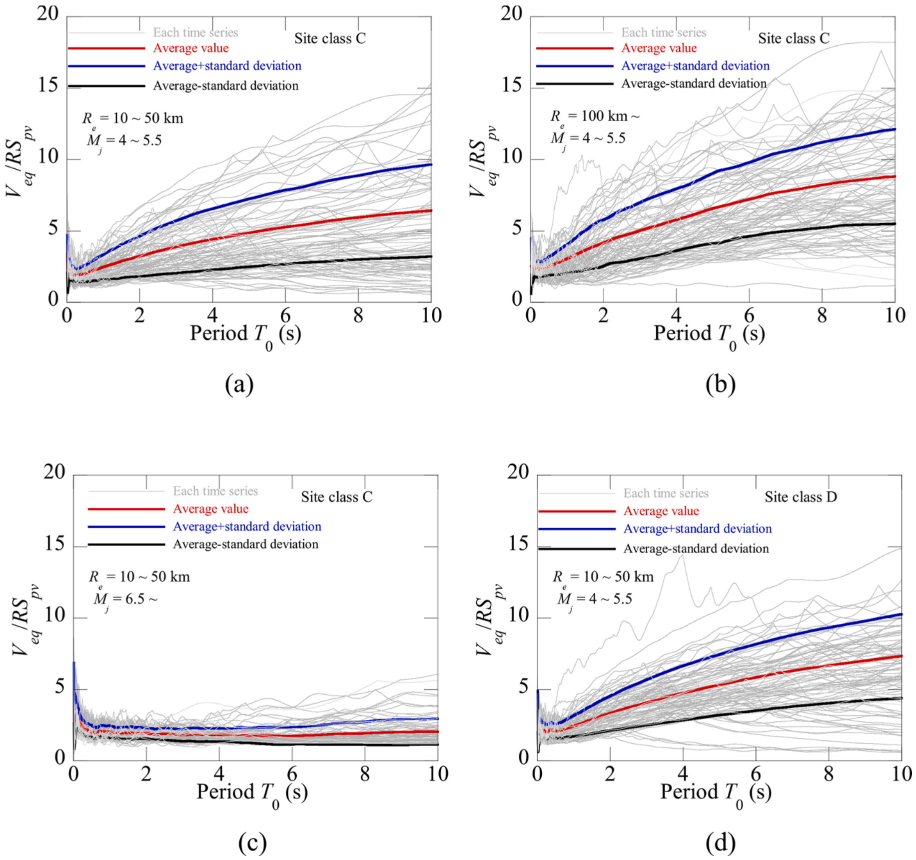

(a)

(b)

(c)

(d)

Fig. 16. The mean ± standard deviation values of V_{eq}/RS_{pv} obtained from seismic records for different cases of magnitude M_j, distance R_e, and site conditions: (a) $M_j = 4$–5.5, $R_e = 10$–50 km, site class C; (b) $M_j = 4$–5.5, $R_e = 100$ km ~, site class C; (c) $M_j = 6.5$ ~, $R_e = 10$–50 km, site class C; and (d) $M_j = 4$–5.5, $R_e = 10$–50 km, site class D.

[26] are typically consistent with those for large magnitudes.

Equation (18) is a function of the oscillator period T_0, frequency-content factor ζ, and site conditions. In Eq. (18), the oscillator damping ξ wasn't set as a variable but a constant value of 5 %. This is because the response spectrum defined in the seismic code generally corresponds to a 5 % damping, and V_{eq} is insensitive to the damping ratio ξ [28]. And one can apply the 5 %-damped V_{eq} obtained from Eq. (18) to construct the hysteretic energy spectrum E_H for EBSD by further using the hysteretic-to-input energy ratio spectrum E_H/E_I and considering the structural damping and hysteretic behavior [7,26].

In addition, it can also be noted from Fig. 13 that V_{eq}/RS_{pv} decreases significantly with an increasing magnitude M_j for long oscillator periods. Fig. 14 shows that when the magnitude M_j is moderate, V_{eq}/RS_{pv} increases with distance R_e, whereas when the magnitude M_j is large, the change in the V_{eq}/RS_{pv} with distance R_e is quite small. Fig. 15 shows that when the magnitude M_j is moderate, V_{eq}/RS_{pv} varies with site conditions, whereas when the magnitude M_j is large, the change in V_{eq}/RS_{pv} with site conditions is also quite small. The variation of V_{eq}/RS_{pv} with distance R_e and site conditions is smaller than that with magnitude M_j. In addition, the mean ± standard deviation values of V_{eq}/RS_{pv} obtained from seismic records are shown in Fig. 16. It can be seen that the standard deviation of V_{eq}/RS_{pv} decreases with increasing moment magnitude M and is not that sensitive to the distance R_e and site conditions. Most of the observed trends of V_{eq}/RS_{pv} from real seismic records are consistent with those obtained using the approach proposed in Section 5.

7. Conclusions

This study developed an approach for estimating the relationship between V_{eq} and the pseudo-velocity response spectrum RS_{pv} based on the random vibration theory. The developed approach was adopted to systematically investigate the influences of magnitude, distance, and site conditions on V_{eq}/RS_{pv}. Based on the derived results, a practical V_{eq}/RS_{pv} formulation considering these influences was developed using 16,660 real seismic ground motions in Japan. The major conclusions of this paper are as follows.

1. The V_{eq}/RS_{pv} results calculated using the proposed approach agree well with those of the traditional time-series analysis.
2. The values of V_{eq}/RS_{pv} for long oscillator periods decreased significantly with an increasing magnitude. The key factor controlling the influence of magnitude on V_{eq}/RS_{pv} is the frequency content of ground motion.
3. V_{eq}/RS_{pv} varies with distance and site conditions when the magnitude is moderate, whereas the changes in V_{eq}/RS_{pv} with distance and site conditions are quite small when the magnitude is large. The variation in V_{eq}/RS_{pv} with distance and site conditions is smaller than that with magnitude.
4. The V_{eq}/RS_{pv} results calculated by the proposed practical formulation agree very well with the results of actual seismic records and are better than those of previous formulations.

CRediT authorship contribution statement

Haizhong Zhang: Conceptualization, Methodology, Writing – original draft, Investigation. **Yan-Gang Zhao:** Visualization, Supervision, Writing – review & editing. **Fang-Wen Ge:** Visualization, Data curation. **Yingchi Fang:** Data curation. **Tsutomu Ochiai:** Visualization.

Declaration of Competing Interest

The authors declare that they have no known competing financial interests or personal relationships that could have appeared to influence the work reported in this paper.

Data availability

Data will be made available on request.

Acknowledgements

The authors want to thank the National Natural Science Foundation of China (grant no. 51738001) for their support.

References

[1] Housner G. Limit design of structures to resist earthquakes. In: Proceedings of the 1st world conference on earthquake engineering, Berkeley, California; 1956.
[2] Choi H, Kim J. Energy-based seismic design of buckling-restrained braced frames using hysteretic energy spectrum. Eng Struct 2006;28(2):304–11.
[3] Habibi A, Chan R, Albermani F. Energy-based design method for seismic retrofitting with passive energy dissipation systems. Eng Struct 2013;46:77–86.
[4] Building Standard Law (BSL). Notification no. 631 of the ministry of land, infrastructure, transport and tourism. Earthquake-Resistant Structural Calculation Based on Energy Balance, Tokyo, Japan; 2005.
[5] Akiyama H, Yang ZY, and Kitamura H. A proposal of design energy spectra allowing for rock and soil conditions. J Struct Const Eng 1993;450:59–69.
[6] Decanini LD, Mollaioli F. Formulation of elastic earthquake input energy spectra. Earthq Eng Struct Dynam 1998;27(12):1503–22.
[7] Decanini LD, Mollaioli F. An energy-based methodology for the assessment of seismic demand. Soil Dyn Earthq Eng 2001;21(2):113–37.
[8] Kuwamura H, Galambos TV. Earthquake load for structural reliability. J Struct Eng 1989;115(6):1446–62.
[9] Kunnath SK, Chai YH. Cumulative damage-based inelastic cyclic demand spectrum. Earthq Eng Struct Dynam 2004;33(4):499–520.
[10] Vahdani R, Gerami M, Vaseghi-Nia MA. The spectra of relative input energy per unit mass of structure for Iranian earthquakes. Int J Civ Eng 2019;17(7):1183–99.
[11] Alıcı FS, Sucuoğlu H. Prediction of input energy spectrum: attenuation models and velocity spectrum scaling. Earthq Eng Struct Dynam 2016;45(13):2137–61.
[12] Alıcı FS, Sucuoğlu H. Elastic and inelastic near-fault input energy spectra. Earthq spectra 2018;34(2):611–37.
[13] Chapman MC. On the use of elastic input energy for seismic hazard analysis. Earthq spectra 1999;15(4):607–35.
[14] Chou C-C, Uang C-M. Establishing absorbed energy spectra-an attenuation approach. Earthq Eng Struct Dynam 2000;29(10):1441–55.
[15] Cheng Y, Lucchini A, Mollaioli F. Proposal of new ground-motion prediction equations for elastic input energy spectra. Earthq Struct 2014;7(4):485–510.
[16] Cheng Y, Lucchini A, Mollaioli F. Ground-motion prediction equations for constant-strength and constant-ductility input energy spectra. Bull Earthq Eng 2020;18(1):37–55.
[17] Gong MS, Xie LL. Study on comparison between absolute and relative input energy spectra and effects of ductility factor. Acta Seismol Sin 2005;18(6):717–26.
[18] Ghodrati Amiri G, Darzi GA, Vaseghi Amiri J. Design elastic input energy spectra based on Iranian earthquakes. Can J Civil Eng 2008;35(6):635–46.
[19] Benavent-Climent A, Pujades LG, López-Almansa F. Design energy input spectra for moderate-seismicity regions. Earthq Eng Struct Dynam 2002;31(5):1151–72.
[20] Benavent-Climent A, López-Almansa F, Bravo-González DA. Design energy input spectra for moderate-to-high seismicity regions based on Colombian earthquakes. Soil Dyn Earthq Eng 2010;30(11):1129–48.
[21] Chai YH, Fajfar P. A procedure for estimating input energy spectra for seismic design. J Earthq Eng 2000;4(4):539–61.
[22] Dindar AA, Yalçın C, Yüksel E, Özkaynak H, Büyüköztürk O. Development of earthquake energy demand spectra. Earthq spectra 2015;31(3):1667–89.
[23] López-Almansa F, Yazgan AU, Benavent-Climent A. Design energy input spectra for high seismicity regions based on Turkish registers. Bull Earthq Eng 2013;11(4):885–912.
[24] Mezgebo MG, Lui EM. Hysteresis and soil site dependent input and hysteretic energy spectra for far-source ground motions. Adv. Civ Eng 2016;2016:1–29.
[25] Riddell R, Garcia JE. Hysteretic energy spectrum and damage control. Earthq Eng Struct Dynam 2001;30(12):1791–816.
[26] Du B, He Z, Wu Y, Huang G, Pan F. A compatible energy demand estimate considering code-specified design spectra. Soil Dyn Earthq Eng 2020;137(8):106273.
[27] ATC. Tentative provisions for the development of seismic regulations for buildings. ATC Publication ATC 3-06, Applied Technology Council, NBS Special Publication 510, NSF Publication 78-8. Washington, DC: U.S. Government Printing Office; 1978.
[28] Akiyama H, Kitamura H. Relationship between energy spectra and velocity response spectra. J Struct Const Eng 2006;71(608):37–43.
[29] Merter O. An investigation on the maximum earthquake input energy for elastic SDOF systems. Earthq Struct 2019;16(4):487–99.
[30] Boore DM. Simulation of ground motion using the stochastic method. Pure Appl Geophys 2003;160(3):635–76.
[31] Boore DM, Thompson EM. Revisions to some parameters used in stochastic-method simulations of ground motion. Bull Seismol Soc Am 2015;105(2A):1029–41.
[32] Wang X, Rathje EM. Influence of peak factors on site amplification from random vibration theory based site-response analysis. Bull Seismol Soc Am 2016;106(4):1733–46.

[33] Cartwright DE and Longuet-Higgins MS. The statistical distribution of the maxima of a random function. Proc R Soc London. Ser A, Math Phys Sci 1956;237:212–32.

[34] Davenport AG. Note on the distribution of the largest value of a random function with application to gust loading. Pro Inst Civ Engrs 1964;28(2):187–96.

[35] Vanmarcke EH. On the distribution of the first-passage time for normal stationary random processes. J Appl Mech 1975;42(1):215–20.

[36] Boore DM, Joyner WB. A note on the use of random vibration theory to predict peak amplitudes of transient signals. Bull Seismol Soc Am 1984;74(5):2035–9.

[37] Boore DM, Thompson EM. Path durations for use in the stochastic-method simulation of ground motions. Bull Seismol Soc Am 2014;104(5):2541–52.

[38] Liu L, Pezeshk S. An improvement on the estimation of pseudoresponse spectral velocity using RVT method. Bull Seismol Soc Am 1999;89(5):1384–9.

[39] Boore DM, Thompson EM. Empirical improvements for estimating earthquake response spectra with random-vibration theory. Bull Seismol Soc Am 2012;102(2):761–72.

[40] Ordaz M, Huerta B, Reinoso E. Exact computation of input-energy spectra from Fourier amplitude spectra. Earthq Eng Struct Dynam 2003;32(4):597–605.

[41] Boore DM. SMSIM - Fortran programs for simulating ground motions from earthquakes: version 2.3 – a revision of OFR 96-80-A. Reston, VA: United States Geological Survey; 2005. Tech. Rep.

[42] Nigam NC, Jennings PC. Calculation of response spectra from strong-motion earthquake records. Bull Seismol Soc Am 1969;59(2):909–22.

[43] NEHRP. Recommended provisions for seismic regulations for new buildings and other structures. Washington, DC: Federal Emergency Management Agency; 2000.

[44] Zhang HZ, Zhao YG. Damping modification factor of acceleration response spectrum considering seismological effects. J Earthq Eng 2021. https://doi.org/10.1080/13632469.2021.1991521.

[45] Strong-motion Seismograph Networks (K-NET, KiK-net). http://www.kyoshinbosai.go.jp/kyoshin/ (accessed on 16 May 2021).

[46] Kanno T, Narita A, Morikawa N, Fujiwara H, Fukushima Y. A new attenuation relation for strong ground motion in Japan based on recorded data. Bull Seismol Soc Am 2006;96(3):879–97.